Carbon Resources Conversion 7 (2024) 100225

Contents lists available at ScienceDirect

Carbon Resources Conversion

journal homepage: www.keaipublishing.com/en/journals/carbon-resources-conversion

Original Article

From food waste to high-capacity hard carbon for rechargeable sodium-ion batteries

Madina Kalibek [a], Lunara Rakhymbay [a], Zhanar Zhakiyeva [a], Zhumabay Bakenov [a], Seung-Taek Myung [b,*], Aishuak Konarov [a,*]

[a] Department of Chemical and Materials Engineering, School of Engineering and Digital Sciences, Nazarbayev University, 53 Kabanbay Batyr Ave., Astana, Kazakhstan
[b] Hybrid Materials Research Center, Department of Nanotechnology and Advanced Materials Engineering, Sejong Battery Institute, Sejong University, Seoul 05006, South Korea

ARTICLE INFO

Keywords:
Coffee waste
Hard carbon
Phosphorus doping
Sodium-ion batteries

ABSTRACT

In this study, we introduce a straightforward and effective approach to produce P-doped hard carbon using coffee grounds as the precursor, with H_3PO_4 serving as the doping agent. By varying the concentrations of H_3PO_4 (1 M, 2 M, and 3 M), we aimed to determine the optimal doping level for maximizing the incorporation of phosphorus ions into the carbon framework. Our investigation revealed that using 2 M of H_3PO_4 as the dopant material for hard carbon led to promising electrochemical performance when employed as an anode material for sodium-ion batteries. The P-doped hard carbon, carbonized at 1300 °C, exhibited an impressive reversible capacity of 341 mAh g^{-1} at a current density of 20 mA g^{-1}, with an initial Coulombic efficiency (ICE) of 83 %. This outstanding electrochemical performance of P-doped hard carbon can be attributed to its unique properties, including a porous agglomerated structure, a significant interlayer spacing, and the formation of C–P bonds.

1. Introduction

The demand for lithium-ion batteries (LIBs) is increasing due to global environmental issues and rising oil prices. The high energy density per weight and volume of LIBs allows their use as power sources not only in portable, but also in stationary grid-scale applications [1–3]. Notwithstanding, uneven distribution and scarcity of lithium resources render us to explore a viable alternative such as sodium-ion batteries (SIBs). Ionic radius (0.072 nm for Li^+ and 0.102 nm for Na^+) and electrode potential (3.04 V vs. standard hydrogen electrode (SHE) for Li^+/Li and 2.71 V vs. SHE for Na^+/Na) are two intrinsic parameters, allowing to distinguish LIBs and SIBs [4]. The electrochemical properties of both storage systems, LIBs and SIBs, directly correlate with cell components (anode, cathode, electrolyte, and separator) [5].

The anode materials for SIBS include chalcogen [6], organic [7], titanium-based compounds [8], and metal-based alloys [9], carbonaceous materials [10] that are widely investigated because they are eco-friendly and chemically stable. Hard carbon (HC) [11] is a promising candidate for carbonaceous materials for SIBs with the following advantages: low cost, low operating voltage (~0 V vs. Na^+/Na), and high capacity (~300 mAh g^{-1}). However, there are some drawbacks such as low initial coulombic efficiency (ICE) and poor rate performance. HC has a similar ion transfer and storage mechanism to graphite and carbon materials (carbon nanotubes, nanofibers, graphene, *etc.*) [12]. In contrast to graphite, HC has a more complicated structure, comprising graphene layers with about 0.37 nm interlayer spacing, amorphous regions, and micropores.

One significant parameter that affects the electrochemical performance is the carbonization temperature [13]. Different precursor materials for hard carbon (synthetic polymers [14], raw biomass [15], and biopolymers [16]) have specific carbonization temperatures for a well-ordered graphene layer formation. HCs prepared at high temperatures (>1200 °C), deliver higher capacity on the plateau than HCs produced at low temperatures (<1000 °C) [17–23]. Generally, high carbonization temperatures lead to lower specific surface areas of the resulting HCs materials, thus decreasing the electrolyte decomposition and the formation of the solid electrolyte interphase (SEI) [24]. The use of raw biomass materials such as corn cob (298 mAh g^{-1} at 0.1C) [25], typha (204.8 mAh g^{-1} at 100 mA g^{-1}) [26], lotus stem (350 mAh g^{-1} at 100 mA g^{-1}) [27], orange peel (156 mAh g^{-1} at 500 mA g^{-1}) [28], and starch (239 mAh g^{-1} at 0.1C) [29] is a promising way for HC synthesis because of the reduced cost due to abundance in nature and eco-

* Corresponding authors.
E-mail addresses: smyung@sejong.ac.kr (S.-T. Myung), aishuak.konarov@nu.edu.kz (A. Konarov).

https://doi.org/10.1016/j.crcon.2024.100225
Received 23 October 2023; Received in revised form 28 December 2023; Accepted 14 January 2024
Available online 23 January 2024

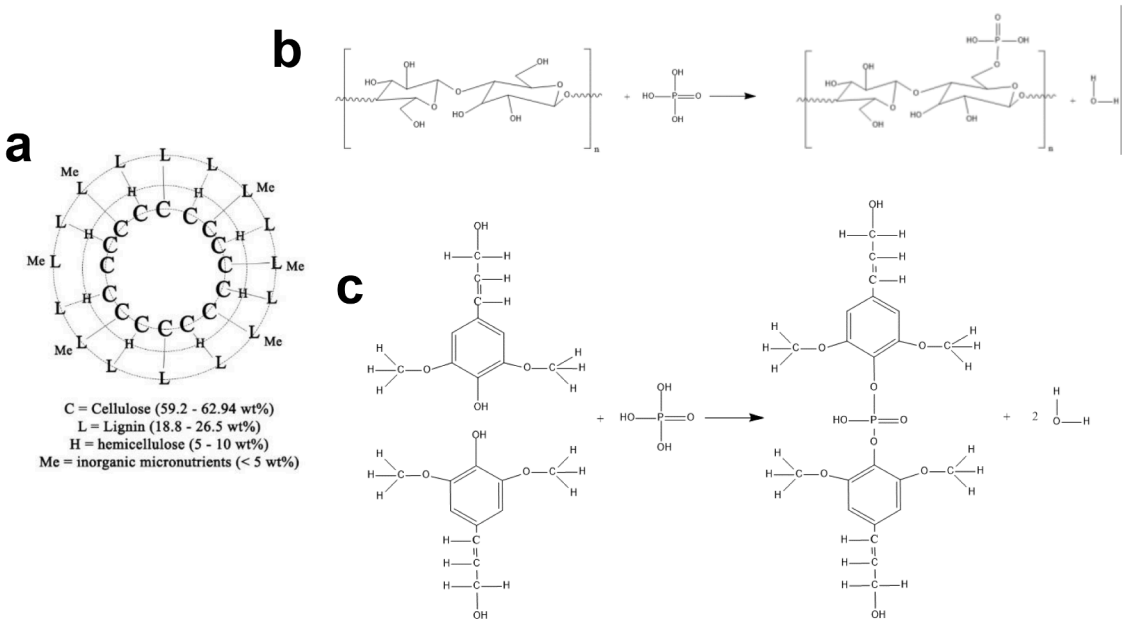

Fig. 1. (a) Physical and chemical characterization of the coffee ground; (b) reaction between cellulose and phosphoric acid; (c) reaction between lignin and phosphoric acid.

friendliness. In this work, we have chosen coffee waste as the precursor for HC synthesis. First reasoning is that annually nearly ~18 million metric tonnes of wet coffee grounds are disposed in landfills, releasing methane gas that affects global warming [30]. The second reasoning is the lignocellulosic structure of the coffee ground waste with high lignin and low inorganic compounds content that form the disordered carbonaceous structure upon carbonization. Generally, ground coffee waste consists of cellulose (59.2–62.94 wt%), hemicellulose (5 –10 wt%), lignin (18.8–26.5 wt%), and inorganic micronutrients (<5 wt%) [31,32]. In particular, the content of cellulose is the highest in comparison with available biowaste materials [33–37]. Improvement of Na^+ diffusivity can be elaborated by heteroatom-dopings (B [36], N [38], O [39], S [19], and P [40]), leading to the dilation of interlayer spacing, porosity enhancement, and defect formation [41]. P - doping is particularly interesting, because C–P bond in HC matrix improves Na^+ diffusivity due to its electro-conducting nature. Wang et al. [42] explained the enhancement of the catalytic activity of P-doped HC due to the dilation of interlayer spacing because of the introduction of large P ions.

Considering above-mentioned facts, we have carbonized the coffee bean waste at 1300 °C through *in situ* P doping. The P-doped HC delivers a high reversible capacity of 341 mAh g^{-1} at 20 mA g^{-1}, with Initial Coulombic efficiency (ICE) of ~ 83 %. And the resulting capacity retention is 80 % (from 1st discharge capacity) for 50 cycles. This excellent electrochemical performance of P-doped HC can be attributed to the effect of P doping that endorses formation of the large interlayer spacing and the conductive network supported by the C–P bond. We herein report on the detailed synthetic process and the related properties of P-doped HC derived from coffee bean wastes.

2. Experimental

2.1. Material synthesis

Hard carbon (HC) was synthesized by a carbonization process using coffee bean waste as a precursor material. Before carbonization, the coffee bean waste was first dried in oven to remove water. Then, the dried coffee bean powder (15 g) was stirred (300 rpm) in diluted hydrochloric acid (0.5 M, 150 ml) solution for 12 h to remove unnecessary water-soluble impurities. After filtering, washing with deionized water until pH 7, and drying at 80 °C for overnight, the obtained brownish powder was slowly stirred (100 rpm) with H_3PO_4 solution for 2 h The solution was filtered and dried at 80 °C for 48 h. Then, the obtained powder was carbonized at 1300 °C in a N_2 atmosphere for 4 h.

2.2. Material characterization.

The morphology of powders were characterized using a scanning electron microscope (SEM, CROSSBEAM 540, CARL ZEISS) and transmission electron microscope (TEM, JEM-1400 PLUS, JEOL). The crystal structure of powders was analyzed by X-ray diffraction (XRD, Rigaku). Raman spectroscopy (LABRAM HR EVOLUTION & OMEGA SCOPE, HORIBA & AIST-NT) was used to examine the degree of carbonization. The surface area was examined by Brunauer-Emmett-Teller (BET, QUANTACHROME INSTRUMENTS). X-ray photoelectron spectroscope (XPS, NEXSA, THERMO SCIENTIFIC) was used to understand chemical state of the produced powders.

2.3. Electrochemical characterization.

The electrode was fabricated by blending the active material, acetylene black, and polyvinylidene fluoride with a weight ratio of 8:1:1 in *N*-methyl-2-pyrrolidone. The prepared slurry was spread on Cu foil and dried in a vacuum oven at 110 °C for 12 h. The dried electrode was punched out of disc (f: 14 mm, ~4 mg cm^{-2}). The electrode was paried with a sodium metal disc, separated by a glass filter, in presence of 1 M $NaPF_6$ in ethylene carbonate (EC) – dimethyl carbonate (DMC) – fluoroethylene carbonate (volume ratio of 49:49:2). The fabricated R2032 coin cells were evaluated by Arbin battery tester in the voltage range of 0.01–2.5 V at 20 mA g^{-1}.

3. Results and discussion

3.1. Structural, Chemical, and morphological characterization

Cellulose, hemicellulose, and lignin with an element of C, H, O, and N decompose in the temperature of 315–400 °C [43], 200–400 °C [44], and 200-400 °C [45], respectively. Regarding the physical characterization of coffee bean grounds, lignin and inorganic micronutrients are located on the outer cell of the biomass. Cellulose is arranged on the inner side, and hemicellulose is randomly oriented between cellulose

Table 1
Elemental analysis results.

Elements	Hard carbon		Phosphorus-doped hard carbon		
	HCG-1300 Bare	HCG-1300 After acid washing	HCG-1300-1C (H_3PO_4) = 1 M	HCG-1300-2C (H_3PO_4) = 2 M	HCG-1300-3C (H_3PO_4) = 3 M
C[1]	91.4	100	98.5	98.3	99.1
S[1]	2.6	0	0	0	0
O[2]	1.6	0	0	0	0
K[3]	1.6	0	0	0	0
Ca[3]	1.2	0	0	0	0
Mg[3]	1	0	0	0	0
P[2]	0.6	0	1.5	1.7	0.9
Si[3]	0	0	0	0	0

[1] CHNS and XPS.
[2] XPS.
[3] ICP-MS.

and lignin (Fig. 1a) [46], for which hydrogen bonds connect cellulose, hemicellulose, and lignin.

Washing process can successfully remove the residual impurities such as S, K, Ca, Mg, and P in coffee beans. Washing the coffee bean with 0.5 M of HCl solution results in the formation of water-soluble salts, which can be readily removed during the filtration process. Thus, the filtered coffee bean has been heated at 1300 °C with H_3PO_4 at different concentrations of; namely, 1 M, 2 M, and 3 M H_3PO_4 denoted as HCG-1300-1, HCG-1300-2, and HCG-1300-3, respectively. The obtained HC powders were chemically analyzed in Table 1. As anticipated, the acidic-treatment clearly removed the residual ingredients. And the H_3PO_4-treatment was available to leave P element in the synthesized HC powders. We schematize the condensation process with P in Fig. 1b. Since the outer shell lignin is the only constituent in the coffee ground that has a C = C double bond in the synapyl alcohol unit, it can be transformed into a C–P bond after the thermal decomposition of the product, which is obtained from the condensation reaction with phosphoric acid (Fig. 1c).

Increase of phosphorus content in the HC results from increased phosphoric acid concentration; namely, 1.5 and 1.7 wt%, for HCG-1300-1 and HCG-1300-2, respectively, according to the result of CHNS analysis (Table 1). However, the value became lower for the sample treated with 3 M H_3PO_4 (P: 0.9 wt%) owing to the destruction of the outer shell in the final product.

As shown in Fig. 2a, all XRD patterns for powders show two broad peaks at around 24° and 43°, corresponding to the (002) and (100) crystallographic planes, respectively. (002) intense peak indicates the carbon interlayer-stacking structure, whereas (100) peak determines the mirroring of the hexagonal carbon structure. Fitting the (002) diffraction peaks of the HCG-1300, HCG-1300-1, HCG-1300-2, and HCG-1300-3, the d_{002} was calculated with the following values of 0.367, 0.371, 0.375, 0.368 nm at the 24.19, 23.98°, 23.7°, and 24.14°, respectively, based on Bragg's equation. The interlayer distance between graphene layers is corroborated with TEM analysis, in which the average d_{002} for HCG-1300-1, HCG-1300-2, and HCG-1300-3 was measured with the following values of 0.362, 0.396, 0.402, 0.375 nm, respectively. Notably, the value of d_{002} of the P-doped coffee ground-derived hard carbon exceeds the d_{002} of graphite (0.335 nm), meaning the free movement of sodium ions between graphene layers. The absence of additional peaks in the XRD pattern proves the purity of the samples. When the concentration of the dopant material was increased from 1 M to 2 M, the broad peak shifted to a lower angle, indicating the expansion of the distance between graphene sheets. The sequential increase of dopant concentration led to the reverse effect.

In Fig. 2b, the Raman spectrum of the samples shows two intense and sharp peaks of the D and G bands. The D-band is named "the defect-

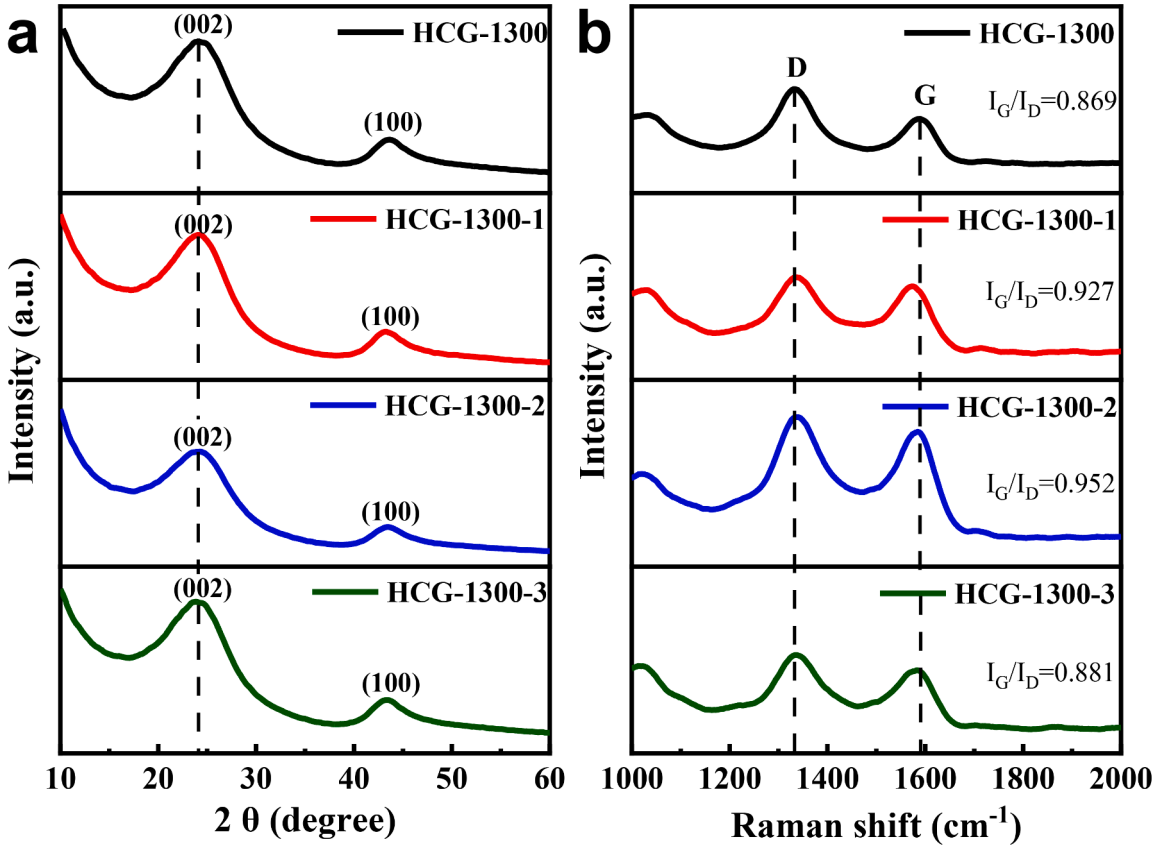

Fig. 2. (a) XRD patterns and (b) Raman spectra of the hard carbons.

Table 2
Calculated crystallographic parameters by XRD and Raman data.

Sample	XRD		Raman		
	2θ (°)	d_{002} (nm)	$I_D I_G^{-1}$	$I_G I_D^{-1}$	$I_D (I_D + I_G)^{-1}$
HCG-1300	24.19	0.367	1.15	0.869	0.507
HCG-1300-1	23.98	0.371	1.078	0.927	0.518
HCG-1300-2	23.7	0.375	1.05	0.952	0.512
HCG-1300-3	24.14	0.368	1.135	0.881	0.531

induced band", which indicates the presence of vacancies, whereas the G-band is named "the crystalline graphite", which corresponds to the graphitic vibrations. The ratio between the D and G bands (I_D/I_G) is the ratio between the degree of defects and graphitization. As mentioned before, $I_D/(I_D + I_G)$ intensity ratio indicates the slope capacity, while I_G/I_D plateau capacity. One may suggest that three regions of the storage mechanism (adsorption, intercalation, and pore-filling) can be considered by the I_D/I_G, d_{002}, and I_G/I_D, respectively (Table 2).

As I_D/I_G indicates the insertion of Na ions into defects, it is logical to point out that a high degree of defects facilitates the easiest adsorption process. At the same time, the increase of graphitization degree promotes the free intercalation of Na ions into nanopores. The expanded d_{002} allows to enhance the intercalation process between graphene sheets. Defect formation in the structure of hard carbon materials results from phosphorus compound evaporation from the sample's surface

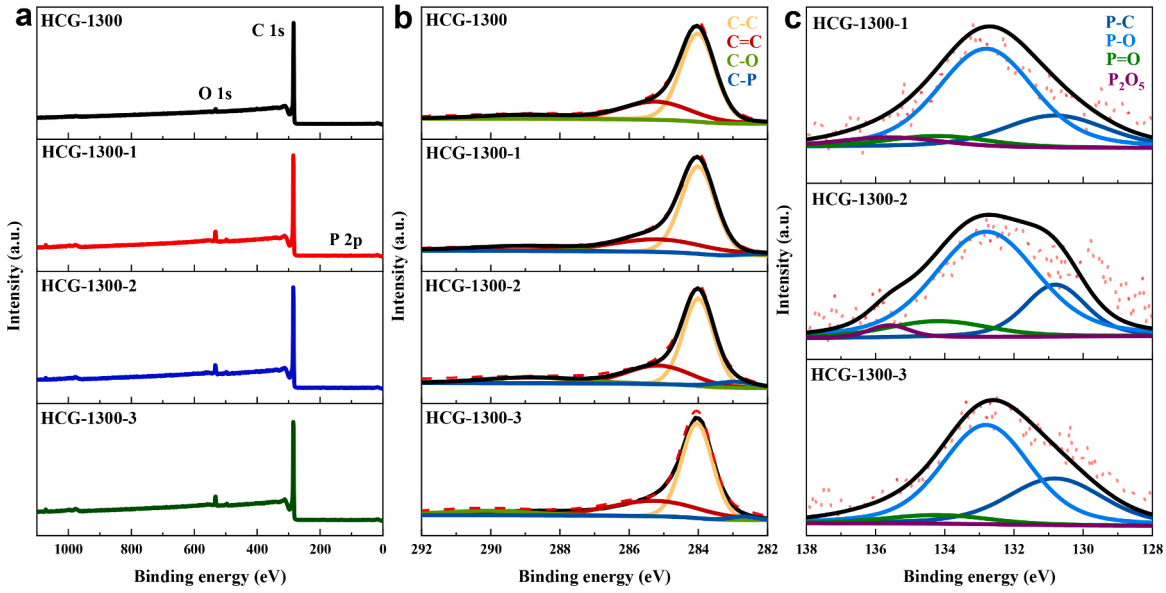

Fig. 3. The XPS spectra of the hard carbons. (a) Full survey XPS, (b) C 1s, and (c) P 2p peaks.

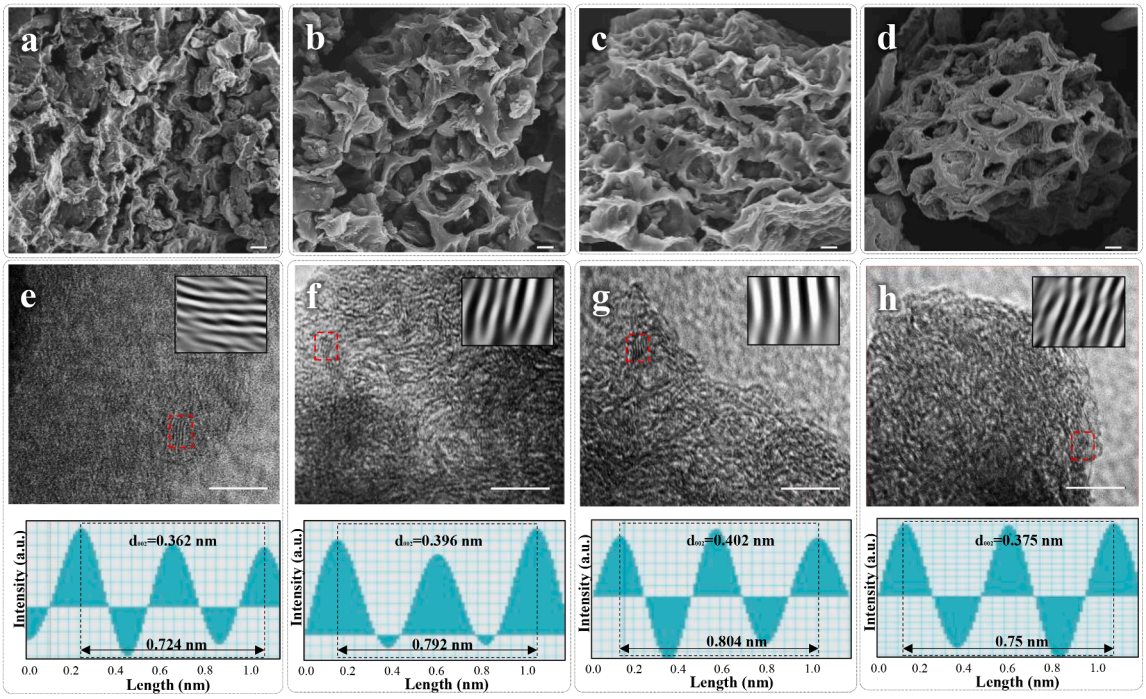

Fig. 4. SEM images of powders: (a) HCG-1300, (b) HCG-1300-1, (c) HCG-1300-2, and (d) HCG-1300-3; TEM images, corresponding FFT images, and distributions of the interlayer spacing of powders: (e) HCG-1300, (f) HCG-1300-1, (g) HCG-1300-2, and (h) HCG-1300-3, respectively.

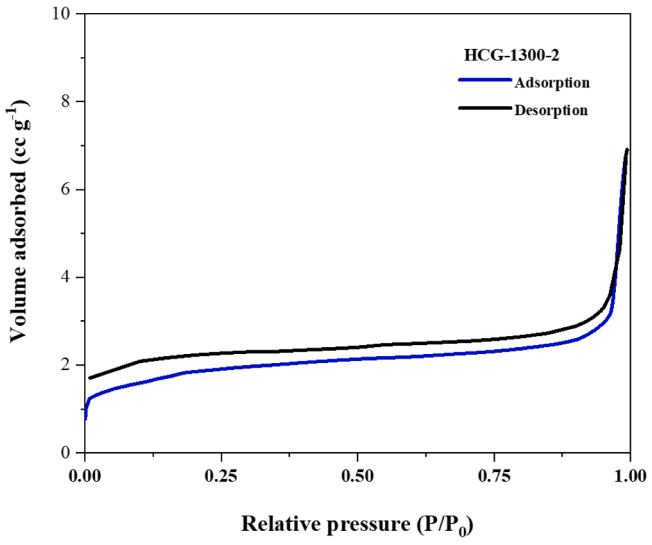

Fig. 5. BET isotherm plot for nitrogen adsorption capacity of the HCG-1300-2.

during the carbonization process. Logically, the defect degree should increase with phosphoric acid concentration. However, the cellulose, the main constituent linked with hemicellulose and lignin by hydrogen bonding, dissolves slowly at high concentrations of H_3PO_4, thus forming a viscous layer that restricts the incorporation of acid into the structure. 1 M of H_3PO_4 destructs the outer shell of the biomass material, forming minor defects. 2 M of H_3PO_4 and 3 M of H_3PO_4 dissolve the exterior dry cellulose powder and form defects on the surface of hard carbon (HCG-1300-3).

XPS analysis was performed to validate the above assumption on the formation of bond and chemical state of the products (Fig. 3). C-C and C = C are the main characteristic bonds for the hard carbon. With an increase in dopant concentration, the atomic ratio for C-C (64.25, 57.04, 60.94 %) and for C═C (25.58, 25.63, and 28.39 %) was obtained. C–O and C–P are the responsible bonds for the enhancement of the electrochemical performance of hard carbons. With an increase in dopant concentration, the atomic ratio for C–O (8.84, 12.21, and 8.85 %) and for C–P (1.33, 5.12, and 1.83 %) was obtained. It is possible to conclude that HCG-1300-2 will have the highest specific capacity among all observed samples.

The scanning electron microscopy (SEM) images of Fig. 4a–d show that the coffee ground-derived hard carbon consists of agglomerated particles with a structural deepening. During the thermal calcination in an inert atmosphere, such gases as H_2O, CO, and CO_2 are released through the coffee ground particles, and the pressure induced by the gas evolution might have led to the crumbling structure. Undoubtedly, this kind of morphology has an advantageous impact on electrolyte incorporation into the structure, enhancing the Na ions transport through the coffee ground carbon electrode.

HCG-1300-1 and HCG-1300-2 have major indentations compared to HCG-1300 due to the evaporation of phosphorus compounds from the surface of hard carbon. Whereas HCG-1300-3 has hollow pores, evidencing the destruction of the lignin outer shell. Hence, SEM analysis can be corroborated with XPS data in Table 2, showing the decrease of the C–P's atomic %.

Fig. 4e-h shows a TEM micrograph of the HCGs. Similarly, results obtained by TEM pointed to 3-dimensional random micron-scale particle sizes and shapes. In addition, some agglomeration of carbon particles was observed. FFT images show a visual representation of graphene layers, the average distances of which were calculated by Gatan Microscopy Suit Software. The average values of d_{002} for HCG-1300, HCG-1300-1, HCG-1300-2, and HCG-1300-3 are 0.362, 0.396, 0.402, and 0.375 nm, respectively. These values can be compared with d_{002} calculated based on XRD data. Graphene layers within hard carbon can be altered in distance, influenced by factors such as carbonization temperature or the presence of doping materials. When this distance increases, diffusibility of sodium ions increases. Consequently, a greater distance corresponds to a higher capacity. However, the distances between graphene sheets are different, depending on which domain is considered. The reduction of the contact between anode and electrolyte could result from the negligible surface area for all samples (<10 m^2 g^{-1}) measured by N_2 adsorption–desorption (Fig. 5).

3.2. Electrochemical performances

The performance of the coffee ground-derived hard carbon was investigated as anode material in half-cell SIBs. Galvanostatic discharge/charge curves of the coffee ground-derived hard carbon are

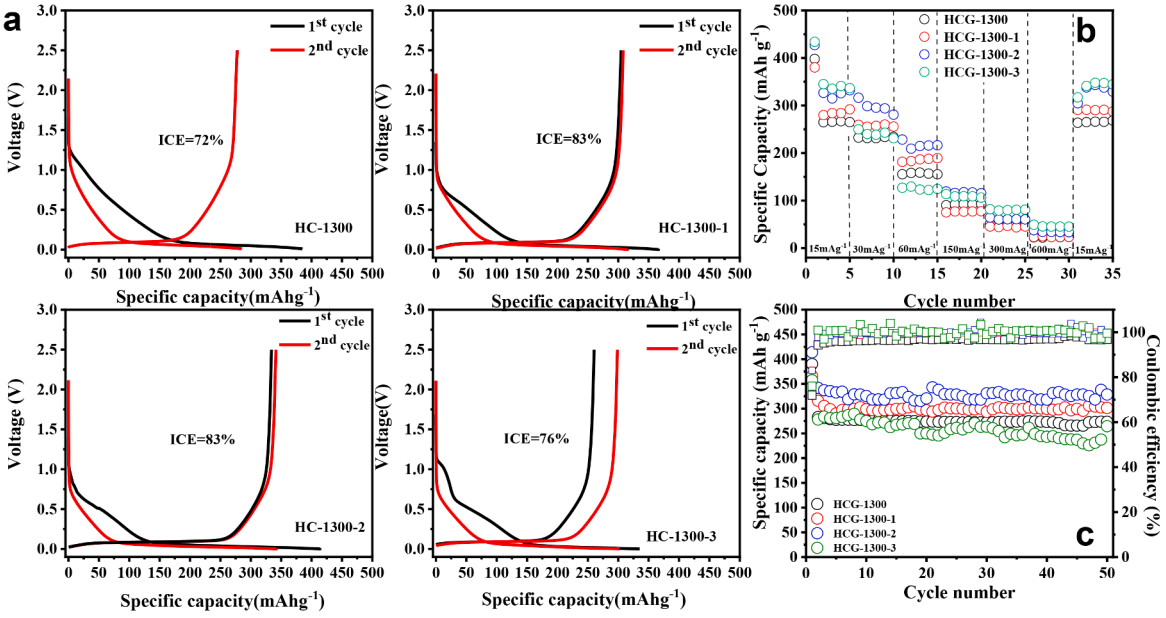

Fig. 6. (a) Electrochemical performance of electrodes. The first and second galvanostatic discharge/charge profiles at 20 mA g^{-1}; (b) rate performance at various current densities; (c) cycling performance at 20 mA g^{-1}.

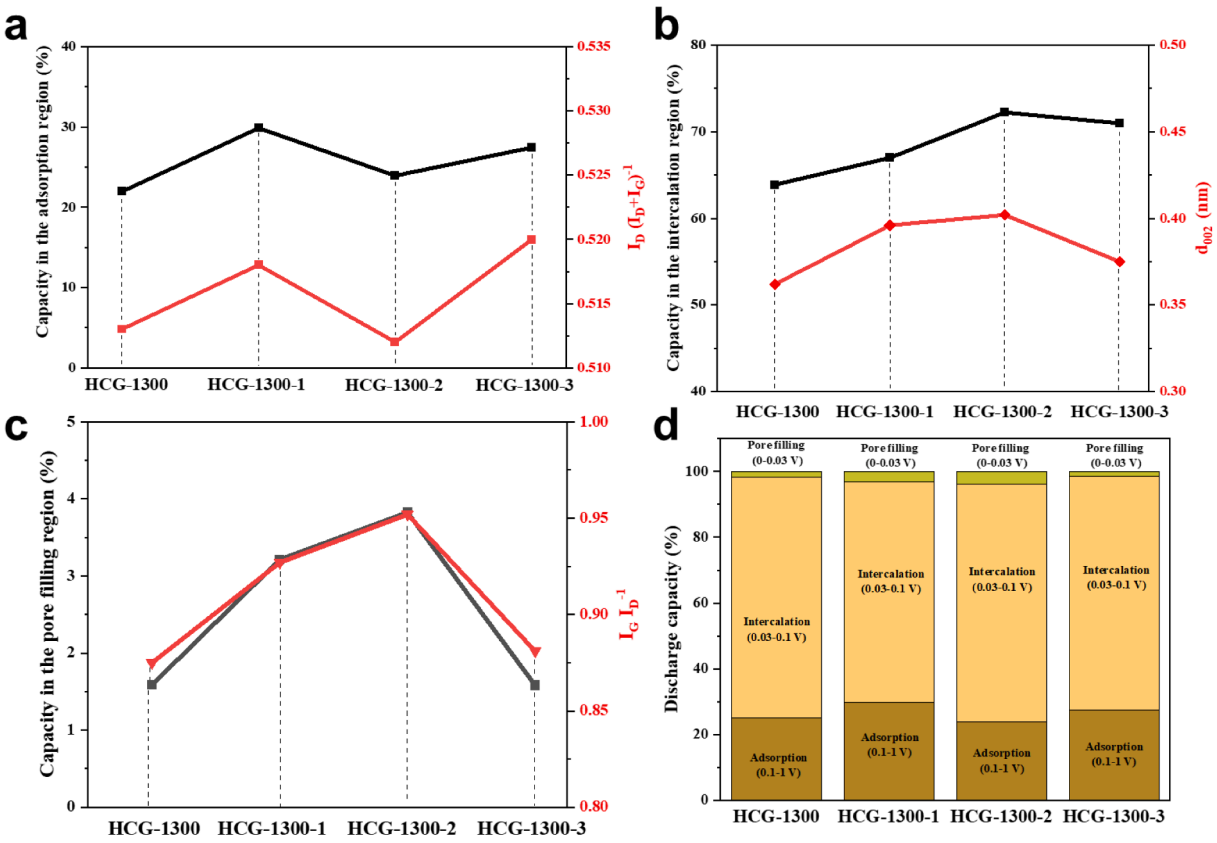

Fig. 7. (a) Capacity in the adsorption region and $I_D (I_D + I_G)^{-1}$, (b) capacity in the intercalation region and d_{002}, and (c) capacity in the pore filling region and $I_G I_D^{-1}$, (d) stacked column of discharge capacity in three storage regions.

shown in Fig. 6a, where the profiles are presented for two cycles at 20 mA g^{-1} (0.07C). The first discharge gives rise to an irreversible capacity of 384, 366, 413, and 340 mAh g^{-1} for HCG-1300, HCG-1300-1, HCG-1300-2, and HCG-1300-3, with the ICE of 72, 83, 83, and 76 %, respectively. In the undoped hard carbon scenario, during the initial charging and discharging cycles, undesirable side reactions with the electrolyte occur, leading to the formation of an unstable solid electrolyte interface (SEI) on the surface and uncompensated Na^+ storage by functional groups of the coffee ground-derived hard carbon. This results in an increased irreversible capacity loss, causing higher polarization and reduced initial coulombic efficiency. Conversely, when hard carbon is doped with phosphoric acid, the surface properties undergo modification, resulting in the formation of a more stable and protective SEI on the electrode surface. This modification reduces side reactions, minimizing irreversible capacity loss and improving overall efficiency during the initial cycles, consequently achieving a higher initial coulombic efficiency. It is likely to note that irreversible capacity mainly came from the adsorbed Na ion. Among tested samples HCG-1300-2 showed the highest ICE due to the negligible surface area (10 m^2 g^{-1}).

After the first cycle, the discharge capacity of HCG tends to saturate to 284, 315, 342, and 305 mAh g^{-1} in HCG-1300, HCG-1300-1, HCG-1300-2, and HCG-1300-3, with the capacity retention for these samples, is 74, 86, 83, and 89 %, respectively.

The rate performance of the hard carbons is shown in Fig. 6b. The cell was discharged and charged at various current densities for five cycles. HCG-1300 delivered a specific capacity of 292, 259, 187, 76, 46, 23 and 290 mA g^{-1} at 0.05, 0.1, 0.2, 0.5, 1, and 2C, respectively. When the current density decreased back to 0.05C, the specific capacity recovered to 290 mA g^{-1}, which shows the stable cycling performance. Fig. 6b shows the rate performance of 1 M phosphorus-doped hard carbon (HCG-1300-1). When the current density increased to 0.5C, the electrode delivered only about 77 mA g^{-1}, while that of 2 M and 3 M P-doped HCGs delivered 117 and 109 mA g^{-1}, respectively.

Fig. 6c displays the cyclic performance of HCG-1300, HCG-1300-1, HCG-1300-2, and HCG-1300-3 at a current density of 20 mA g^{-1} (0.07C). After 50 cycles, coffee ground-derived hard carbon (HCG-1300) retains a reversible capacity of 273 mAh g^{-1}, corresponding to a capacity retention of 70 % due to the less active reaction sites. While, P-doped coffee ground-derived hard carbons (HCG-1300-1, HCG-1300-2, HCG-1300-3) exhibit much higher capacity, i.e., about 302, 338, and 264 mAh g^{-1}, respectively, after 50 cycles at 20 mA g^{-1} (Capacity retention: 83, 82, and 74 %, respectively). These results demonstrate that the rate performance and cycling of carbon material derived from the coffee ground can be greatly improved by H_3PO_4 activation. The HCG-1300-2 shows a superior rate and cycling performance than the previously reported coffee ground-derived carbon materials [19,40,41,46,47].

Fig. 6a–d illustrate the relationship between a material's adsorption, intercalation, and pore-filling capacities, and their corresponding indicators: $I_D/(I_D + I_G)^{-1}$, d_{002}, and I_G/I_D. It is important to highlight the role of lignin in this context, which possesses double bonds susceptible to breakage, aiding in the formation of C–P bonds. In the case of HCG-1300-3, the reduced d_{002} and elevated $I_D/(I_D + I_G)$ values are attributed to the absence of lignin, resulting from the destruction of the outer shell.

In Fig. 6a, a high degree of defects facilitates the adsorption process. After introducing dopants to HCG-1300, the $I_D/(I_D + I_G)$ value for HCG-1300-1 increases due to dopant evaporation. Subsequently, a 2 M concentration promotes significant interaction with biomass, shifting the main influence towards C–P bond formation and elevating d_{002}. In HCG-1300-2, a substantial portion of the dopant contributes to C–P bond formation, with a smaller amount dedicated to surface defect formation, reflected in the lower $I_D/(I_D + I_G)$ compared to HCG-1300-1. The increase in $I_D/(I_D + I_G)$ for HCG-1300-3 is associated with structural

degradation rather than dopant evaporation, emphasizing the nuanced impact of dopant interactions and structural changes.

In Fig. 6b, the expanded d_{002} enhances the intercalation process between graphene sheets. The increase occurs until HCG-1300-2 due to C–P bond formation, after which it decreases for HCG-1300-3 due to the destructuring of the outer shell, where lignin plays a crucial role.

In Fig. 6c, a well-organized pore structure facilitates graphitization by providing ordered pathways for carbon atom rearrangement during pyrolysis. Low to moderate dopant concentrations may promote graphitization, while high concentrations can lead to structural disruption and a subsequent decrease in the degree of graphitization. Practical measurements have proved the theoretical assumption. Hence, the specific capacity in three regions has the following dependencies: capacity in the adsorption region with the ratio between I_D $(I_D + I_G)^{-1}$, the capacity in the intercalation region with the d_{002}, the capacity in the pore filling region with the I_G/I_D.

The discharge capacity for HCG-1300, HCG-1300-1, HCG-1300-2 and HCG-1300-3 in three storage regions are presented in Fig. 7d. It is seen that HCG-1300-2 has the highest discharge in the intercalation and pore-filling region, correlating with XPS analysis. Therefore, 2 M of H_3PO_4 is the most appropriate concentration for phosphorus incorporation into the carbon matrix.

4. Conclusion

In summary, this study involved the synthesis of P-doped hard carbon using coffee grounds and phosphoric acid, followed by filtration to remove unabsorbed PO_4^{3-} ions, and carbonization at a high temperature of 1300 °C. The resulting hard carbons exhibited a distinctive honeycomb structure derived from the pyrolysis of coffee grounds, creating numerous open cavities that facilitate efficient ion transmission and electrolyte penetration. Notably, the incorporation of phosphorus dopants played a pivotal role in enhancing the electrochemical performance of these materials. The synthesized HCG-1300-2 demonstrated an exceptional specific capacity of 341 mAh g^{-1} with an initial Coulombic efficiency of 83 % at a current density of 20 mA g^{-1}, owing to the efficient integration of phosphorus ions into the carbon framework. Furthermore, a detailed examination of the relationship between microstructure and electrochemical performance revealed that P-doping led to an increase in d_{002} spacing and the introduction of more defects and pores into the material's structure. This work underscores the significance of P-doping as a means to significantly enhance the electrochemical performance of hard carbon. The P-doped hard carbon material shows promise as a compelling candidate for anode applications in sodium-ion batteries (SIBs).

CRediT authorship contribution statement

Madina Kalibek: Data collection, Visualization, Validation, Writing – review & editing. **Lunara Rakhymbay:** Conceptualization, Writing – review & editing. **Zhanar Zhakiyeva:** Validation, Investigation, Writing – review & editing. **Zhumabay Bakenov:** Validation, Writing – review & editing. **Seung-Taek Myung:** Writing – review & editing, Visualization, Validation, Supervision. **Aishuak Konarov:** Writing – review & editing, Visualization, Validation, Supervision, Resources, Funding acquisition, Conceptualization.

Declaration of competing interest

The authors declare that they have no known competing financial interests or personal relationships that could have appeared to influence the work reported in this paper.

Acknowledgement

This work was funded by the Ministry of Education and Science of the Republic of Kazakhstan Grant (AP09259165) and by Nazarbayev University under Collaborative Research Program Grant № 20122022P1611, AK.

References

[1] J.-Y. Hwang, S.-T. Myung, Y.-K. Sun, Sodium-ion batteries: present and future, Chem. Soc. Rev. 46 (2017) 3529–3614, https://doi.org/10.1039/C6CS00776G.
[2] N. Yabuuchi, K. Kubota, M. Dahbi, S. Komaba, Research development on sodium-ion batteries, Chem. Rev. 114 (2014) 11636–11682, https://doi.org/10.1021/cr500192f.
[3] C. Vaalma, D. Buchholz, M. Weil, S. Passerini, A cost and resource analysis of sodium-ion batteries, Nat. Rev. Mater. 3 (2018) 18013, https://doi.org/10.1038/natrevmats.2018.13.
[4] B. Xiao, T. Rojo, X. Li, Hard Carbon as sodium-ion battery anodes: progress and challenges, ChemSusChem. 12 (2019) 133–144, https://doi.org/10.1002/cssc.201801879.
[5] W. Tang, Y. Zhang, Y. Zhong, T. Shen, X. Wang, X. Xia, J. Tu, Natural biomass-derived carbons for electrochemical energy storage, Mater. Res. Bull. 88 (2017) 234–241, https://doi.org/10.1016/j.materresbull.2016.12.025.
[6] Z. Ali, T. Zhang, M. Asif, L. Zhao, Y. Yu, Y. Hou, Transition metal chalcogenide anodes for sodium storage, Mater. Today. 35 (2020) 131–167, https://doi.org/10.1016/j.mattod.2019.11.008.
[7] C. Luo, J.J. Shea, J. Huang, A carboxylate group-based organic anode for sustainable and stable sodium ion batteries, J. Power Sources 453 (2020) 227904, https://doi.org/10.1016/j.jpowsour.2020.227904.
[8] S. Guo, J. Yi, Y. Sun, H. Zhou, Recent advances in titanium-based electrode materials for stationary sodium-ion batteries, Energy Environ. Sci. 9 (2016) 2978–3006, https://doi.org/10.1039/C6EE01807F.
[9] G. Yang, P.R. Ilango, S. Wang, M.S. Nasir, L. Li, D. Ji, Y. Hu, S. Ramakrishna, W. Yan, S. Peng, Carbon-based alloy-type composite anode materials toward sodium-ion batteries, Small 15 (2019) 1900628, https://doi.org/10.1002/smll.201900628.
[10] Y. Lu, K.H. Shin, Y. Yu, Y. Hu, J. Liang, K. Chen, H. Yuan, H.S. Park, D. Wang, Multiple active sites carbonaceous anodes for na $^{+}$ storage: synthesis, electrochemical properties and reaction mechanism analysis, Adv. Funct. Mater. 31 (2021) 2007247, https://doi.org/10.1002/adfm.202007247.
[11] E. Irisarri, A. Ponrouch, M.R. Palacin, Review—hard carbon negative electrode materials for sodium-ion batteries, J. Electrochem. Soc. 162 (2015) A2476–A2482, https://doi.org/10.1149/2.0091514jes.
[12] M.-M. Titirici, R.J. White, N. Brun, V.L. Budarin, D.S. Su, F. Del Monte, J.H. Clark, M.J. MacLachlan, Sustainable carbon materials, Chem. Soc. Rev. 44 (2015) 250–290, https://doi.org/10.1039/C4CS00232F.
[13] S. Alvin, D. Yoon, C. Chandra, R.F. Susanti, W. Chang, C. Ryu, J. Kim, Extended flat voltage profile of hard carbon synthesized using a two-step carbonization approach as an anode in sodium ion batteries, J. Power Sources 430 (2019) 157–168, https://doi.org/10.1016/j.jpowsour.2019.05.013.
[14] Q. Zhang, X. Deng, M. Ji, Y. Li, Z. Shi, Hard carbon microspheres derived from resorcinol formaldehyde resin as high-performance anode materials for sodium-ion battery, Ionics 26 (2020) 4523–4532, https://doi.org/10.1007/s11581-020-03585-7.
[15] Z. Zhu, F. Liang, Z. Zhou, X. Zeng, D. Wang, P. Dong, J. Zhao, S. Sun, Y. Zhang, X. Li, Expanded biomass-derived hard carbon with ultra-stable performance in sodium-ion batteries, J. Mater. Chem. A 6 (2018) 1513–1522, https://doi.org/10.1039/C7TA07951F.
[16] X. Lin, Y. Liu, H. Tan, B. Zhang, Advanced lignin-derived hard carbon for Na-ion batteries and a comparison with Li and K ion storage, Carbon 157 (2020) 316–323, https://doi.org/10.1016/j.carbon.2019.10.045.
[17] H. Wang, Z. Wu, F. Meng, D. Ma, X. Huang, L. Wang, X. Zhang, Nitrogen-doped porous carbon nanosheets as low-cost, high-performance anode material for sodium-ion batteries, ChemSusChem. 6 (2013) 56–60, https://doi.org/10.1002/cssc.201200680.
[18] W. Li, M. Zhou, H. Li, K. Wang, S. Cheng, K. Jiang, A high performance sulfur-doped disordered carbon anode for sodium ion batteries, Energy Environ. Sci. 8 (2015) 2916–2921, https://doi.org/10.1039/C5EE01985K.
[19] L. Qie, W. Chen, X. Xiong, C. Hu, F. Zou, P. Hu, Y. Huang, Sulfur-doped carbon with enlarged interlayer distance as a high-performance anode material for sodium-ion batteries, Adv. Sci. 2 (2015), https://doi.org/10.1002/advs.201500195.
[20] P. Wang, B. Qiao, Y. Du, Y. Li, X. Zhou, Z. Dai, J. Bao, Fluorine-doped carbon particles derived from lotus petioles as high-performance anode materials for sodium-ion batteries, J. Phys. Chem. C 119 (2015) 21336–21344, https://doi.org/10.1021/acs.jpcc.5b05443.
[21] J. Jeon, L. Zhang, J.L. Lutkenhaus, D.D. Laskar, J.P. Lemmon, D. Choi, M. I. Nandasiri, A. Hashmi, J. Xu, R.K. Motkuri, C.A. Fernandez, J. Liu, M.P. Tucker, P. B. McGrail, B. Yang, S.K. Nune, Controlling porosity in lignin-derived nanoporous carbon for supercapacitor applications, ChemSusChem. 8 (2015) 428–432, https://doi.org/10.1002/cssc.201402621.
[22] T. Yang, T. Qian, M. Wang, X. Shen, N. Xu, Z. Sun, C. Yan, A sustainable route from biomass byproduct okara to high content nitrogen-doped carbon sheets for efficient sodium ion batteries, Adv. Mater. 28 (2016) 539–545, https://doi.org/10.1002/adma.201503221.
[23] G. Zou, C. Wang, H. Hou, C. Wang, X. Qiu, X. Ji, Controllable interlayer spacing of sulfur-doped graphitic carbon nanosheets for fast sodium-ion batteries, Small 13 (2017) 1700762, https://doi.org/10.1002/smll.201700762.

[24] A. Kamiyama, K. Kubota, D. Igarashi, Y. Youn, Y. Tateyama, H. Ando, K. Gotoh, S. Komaba, MgO-template synthesis of extremely high capacity hard carbon for Na-ion battery, Angew. Chem. Int. Ed. 60 (2021) 5114–5120, https://doi.org/10.1002/anie.202013951.
[25] P. Liu, Y. Li, Y.-S. Hu, H. Li, L. Chen, X. Huang, A waste biomass derived hard carbon as a high-performance anode material for sodium-ion batteries, J. Mater. Chem. A 4 (2016) 13046–13052, https://doi.org/10.1039/C6TA04877C.
[26] Y. Shen, S. Sun, M. Yang, X. Zhao, Typha-derived hard carbon for high-performance sodium ion storage, J. Alloys Compd. 784 (2019) 1290–1296, https://doi.org/10.1016/j.jallcom.2019.01.021.
[27] N. Zhang, Q. Liu, W. Chen, M. Wan, X. Li, L. Wang, L. Xue, W. Zhang, High capacity hard carbon derived from lotus stem as anode for sodium ion batteries, J. Power Sources 378 (2018) 331–337, https://doi.org/10.1016/j.jpowsour.2017.12.054.
[28] J. Xiang, W. Lv, C. Mu, J. Zhao, B. Wang, Activated hard carbon from orange peel for lithium/sodium ion battery anode with long cycle life, J. Alloys Compd. 701 (2017) 870–874, https://doi.org/10.1016/j.jallcom.2017.01.206.
[29] A.A. Arie, K. Hazel, H. Kristianto, H. Muljana, L. Stievano, Ganyong Starch derived hard carbon anodes for sodium ion batteries, J. Nanosci. Nanotechnol. 21 (2021) 4033–4036, https://doi.org/10.1166/jnn.2021.19220.
[30] Harnessing the power of spent coffee grounds for weight loss, Bio Bean. (n.d.). https://www.bio-bean.com/news-post/zero-waste-week-no-such-thing-as-waste-coffee/ (accessed October 24, 2023).
[31] D. Pujol, C. Liu, J. Gominho, M.À. Olivella, N. Fiol, I. Villaescusa, H. Pereira, The chemical composition of exhausted coffee waste, Ind. Crops Prod. 50 (2013) 423–429, https://doi.org/10.1016/j.indcrop.2013.07.056.
[32] N.E. Dávila-Guzmán, F. De Jesús Cerino-Córdova, E. Soto-Regalado, J.R. Rangel-Mendez, P.E. Díaz-Flores, M.T. Garza-Gonzalez, J.A. Loredo-Medrano, Copper biosorption by spent coffee ground: equilibrium, kinetics, and mechanism, CLEAN – Soil Air Water. 41 (2013) 557–564, https://doi.org/10.1002/clen.201200109.
[33] A. Gomez-Martin, J. Martinez-Fernandez, M. Ruttert, M. Winter, T. Placke, J. Ramirez-Rico, Correlation of structure and performance of hard carbons as anodes for sodium ion batteries, Chem. Mater. 31 (2019) 7288–7299, https://doi.org/10.1021/acs.chemmater.9b01768.
[34] Z. Xu, J. Chen, M. Wu, C. Chen, Y. Song, Y. Wang, Effects of different atmosphere on electrochemical performance of hard carbon electrode in sodium ion battery, Electron. Mater. Lett. 15 (2019) 428–436, https://doi.org/10.1007/s13391-019-00143-w.
[35] J. Fondard, E. Irisarri, C. Courrèges, M.R. Palacin, A. Ponrouch, R. Dedryvère, SEI composition on hard carbon in Na-ion batteries after long cycling: influence of salts ($NaPF_6$, NaTFSI) and additives (FEC, DMCF), J. Electrochem. Soc. 167 (7) (2020) 070526.
[36] M.E. Lee, H.W. Kwak, H.-J. Jin, Y.S. Yun, Waste beverage coffee-induced hard carbon granules for sodium-ion batteries, ACS Sustain. Chem. Eng. 7 (2019) 12734–12740, https://doi.org/10.1021/acssuschemeng.9b00971.
[37] E.M. Lotfabad, J. Ding, K. Cui, A. Kohandehghan, W.P. Kalisvaart, M. Hazelton, D. Mitlin, High-density sodium and lithium ion battery anodes from banana peels, ACS Nano. 8 (2014) 7115–7129, https://doi.org/10.1021/nn502045y.
[38] K. Schutjajew, J. Pampel, W. Zhang, M. Antonietti, M. Oschatz, Influence of pore architecture and chemical structure on the sodium storage in nitrogen-doped hard carbons, Small 17 (2021) 2006767, https://doi.org/10.1002/smll.202006767.
[39] C. Chen, Y. Huang, Z. Meng, J. Zhang, M. Lu, P. Liu, T. Li, Insight into the rapid sodium storage mechanism of the fiber-like oxygen-doped hierarchical porous biomass derived hard carbon, J. Colloid Interface Sci. 588 (2021) 657–669, https://doi.org/10.1016/j.jcis.2020.11.058.
[40] S. Alvin, C. Chandra, J. Kim, Extended plateau capacity of phosphorus-doped hard carbon used as an anode in Na- and K-ion batteries, Chem. Eng. J. 391 (2020) 123576, https://doi.org/10.1016/j.cej.2019.123576.
[41] Z. Pei, Q. Meng, L. Wei, J. Fan, Y. Chen, C. Zhi, Toward efficient and high rate sodium-ion storage: A new insight from dopant-defect interplay in textured carbon anode materials, Energy Storage Mater. 28 (2020) 55–63, https://doi.org/10.1016/j.ensm.2020.02.033.
[42] X. Wang, M. Hou, Z. Shi, X. Liu, I. Mizota, H. Lou, B. Wang, X. Hou, Regulate phosphorus configuration in high p-doped hard carbon as a superanode for sodium storage, ACS Appl. Mater. Interfaces 13 (2021) 12059–12068, https://doi.org/10.1021/acsami.0c23165.
[43] Y.-C. Lin, J. Cho, G.A. Tompsett, P.R. Westmoreland, G.W. Huber, Kinetics and mechanism of cellulose pyrolysis, J. Phys. Chem. C 113 (2009) 20097–20107, https://doi.org/10.1021/jp906702p.
[44] S. Wang, B. Ru, H. Lin, Z. Luo, Degradation mechanism of monosaccharides and xylan under pyrolytic conditions with theoretic modeling on the energy profiles, Bioresour. Technol. 143 (2013) 378–383, https://doi.org/10.1016/j.biortech.2013.06.026.
[45] H. Kawamoto, Lignin pyrolysis reactions, J. Wood Sci. 63 (2017) 117–132, https://doi.org/10.1007/s10086-016-1606-z.
[46] J.P. Paraknowitsch, A. Thomas, Doping carbons beyond nitrogen: an overview of advanced heteroatom doped carbons with boron, sulphur and phosphorus for energy applications, Energy Environ. Sci. 6 (2013) 2839, https://doi.org/10.1039/c3ee41444b.
[47] Z. Li, C. Bommier, Z.S. Chong, Z. Jian, T.W. Surta, X. Wang, Z. Xing, J. C. Neuefeind, W.F. Stickle, M. Dolgos, P.A. Greaney, X. Ji, Mechanism of Na-ion storage in hard carbon anodes revealed by heteroatom doping, Adv. Energy Mater. 7 (2017) 1602894, https://doi.org/10.1002/aenm.201602894.